Materials and Interfaces

Scilight

Article

Check for updates

Au-Fe Separates Enable CO-Assisted Methane Oxidation to Acetic Acid with O_2 via Tandem Catalysis

Hongfei Lin [1], Haibin Yin [1,*], Chuyue Meng [1], Chengyuan Liu [2], Long Zhao [2], Hongliang Li [1], Bo Wu [1,3,*], and Jie Zeng [1,4,5,*]

[1] Hefei National Research Center for Physical Sciences at the Microscale, CAS Key Laboratory of Strongly-Coupled Quantum Matter Physics, Key Laboratory of Surface and Interface Chemistry and Energy Catalysis of Anhui Higher Education Institutes, Department of Chemical Physics, University of Science and Technology of China, Hefei 230026, China
[2] National Synchrotron Radiation Laboratory, University of Science and Technology of China, Hefei, 230026, China
[3] Oxide & Organic Nanomaterials for Energy & Environment Laboratory, Chemistry Program, Physical Science & Engineering, King Abdullah University of Science and Technology, Thuwal 23955, Saudi Arabia
[4] School of Chemistry & Chemical Engineering, Anhui University of Technology, Ma'anshan 243002, China
[5] Deep Space Exploration Laboratory, Hefei 230088, China
* Correspondence: yinhb@ustc.edu.cn (H.Y.); bo.wu@kaust.edu.sa (B.W.); zengj@ustc.edu.cn (J.Z.)
Received: 9 June 2026; Revised: 23 June 2026; Accepted: 28 June 2026; Published: 30 June 2026

Abstract: Direct conversion of methane to acetic acid with molecular O_2 at room temperature remains as a grand challenge. Herein, we achieved room-temperature oxidation of CH_4 into acetic acid with O_2 and CO over structurally optimized Au/TiO_2 and Fe/ZSM-5 through tandem catalysis. The process decouples H_2O_2 formation and migration, H_2O_2 activation to hydroxyl radicals for CH_4 oxidation, and carbon-carbon coupling to acetic acid. The physical mixture of Au/TiO_2 and Fe/ZSM-5 yielded 55.6 μmol g_{cat}^{-1} with the acetic acid selectivity in liquid of 64.9% in H_2O under 61 bar (CH_4:CO:O_2 = 15:40:6) at 30 °C for 6 h without any external energy. *In situ* synchrotron-based vacuum ultraviolet photoionization mass spectrometry demonstrates a closer spatial interval is critical for *in situ* generated H_2O_2 migrates from Au/TiO_2 to Fe/ZSM-5, which can be readily used by Fe/ZSM-5 to produce hydroxyl radicals, enabling the maximum liquid-phase product accumulation.

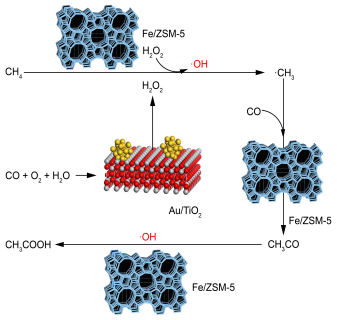

Keywords: methane oxidation; acetic acid; hydroxyl radicals; tandem catalysis

1. Introduction

Direct conversion of methane to methanol with O_2 ($CH_4 + 1/2\ O_2 \rightarrow CH_3OH$) at room temperature remains a grand challenge due to the chemical inertness of both CH_4 and O_2 [1–4]. In nature, methane monooxygenase (MMO), including soluble MMO (sMMO) and particulate MMO (pMMO), efficiently catalyzes this reaction at room temperature [5–7]. The enzymatic processes inspired the researchers to construct partially reduced metal sites [8,9]. Converting methane to acetic acid via a carbon-carbon coupling pathway with O_2 at room temperature is highly challenging, typically requiring elevated temperatures (≥80 °C) or strong oxidants such as H_2O_2 or $K_2S_2O_8$ [10–21].

Room-temperature conversion of methane into acetic acid necessitates external energy sources including light [22], plasma, and γ-ray radiation. Under UV irradiation, photoexcited electrons from TiO_2 moved to Pt/NPW clusters, while holes on TiO_2 reacted with H_2O to produce hydroxyl radical (·OH). These ·OH radicals activated methane and reacted with CO adsorbed on Pt sites, forming acetyl groups oxidized to acetic acid [23]. Using dielectric barrier discharge plasma over Cu/γ-Al_2O_3, the reaction of $CO_2(v) + H \rightarrow CO + OH$ could be one of the major routes for ·OH radicals formation, collectively forming acetic acid from methyl radicals, CO, and ·OH radicals [24]. Under γ-rays, H_2O radiolysis produced ·OH radicals and hydrated electrons, interacting with CH_4 and CO_2 to form methyl and $\cdot CO_2^-$ radicals, coupling into acetic acid [25]. Based on these findings, successfully converting methane to acetic acid at room temperature depended critically on generating reactive hydroxyl radicals.

Based on previous findings, our focus shifts to addressing the key challenge of efficiently generating and utilizing hydroxyl radicals at room temperature. To tackle this, we propose a tandem catalytic strategy that integrates two functions, constructing components capable of efficient H_2O_2 synthesis at room conditions and enabling the efficient utilization of *in situ* generated H_2O_2 to produce hydroxyl radicals for subsequent methane oxidation. By investigating the proximity and interaction between these components, we aim to maximize the overall efficiency of methane selective oxidation to acetic acid. We demonstrate that tandem catalysis enables efficient methane oxidation to acetic acid with O_2 at room temperature without external energy input. Using a physical mixture of Au/TiO_2 and Fe/ZSM-5 catalysts, we achieved 55.6 μmol g_{cat}^{-1} acetic acid yield with 64.9% selectivity in aqueous solution under mild conditions (61 bar, 30 °C, 6 h, CH_4:CO:O_2 = 15:40:6). *In situ* synchrotron-based vacuum ultraviolet photoionization mass spectrometry reveals that close spatial proximity between catalysts is essential for efficient migration of *in situ* generated H_2O_2 from Au/TiO_2 to Fe/ZSM-5, where it decomposes into hydroxyl radicals for subsequent methane oxidation, thereby maximizing liquid-phase product formation.

2. Experimental Section

2.1. Catalyst Preparation

TiO_2 was synthesized using a hydrothermal method. In a typical procedure, 1.8 g of $CO(NH_2)_2$ and 30 mL of Titanium(IV) bis(ammonium lactato) dihydroxide solution (TALH) were dissolved in 270 mL of deionized water. After stirring at room temperature for 30 min, the solution was transferred to a 200-mL Teflon-lined autoclave. The autoclave was then heated to 160 °C and maintained at this temperature for 24 h. The resulting precipitate was collected by centrifugation, washed thoroughly with deionized water, and subsequently dried in an oven at 80 °C for 12 h. The dried powders were ground and calcined in a muffle furnace, heating from room temperature to 300 °C at a ramp rate of 10 °C min^{-1}, and held at 300 °C for 3 h.

Au/TiO_2 was prepared using the deposition-precipitation method, employing NaOH aqueous solution to control the pH. In a typical synthesis, 2.5 g of TiO_2 dispersed in 200 mL of deionized water was mixed with 2.1 mL of $HAuCl_4$ aqueous solution (23.5 g_{Au} L^{-1}) in a beaker, stirred at 750 rpm for 30 min. Subsequently, 17.0 mL of NaOH aqueous solution (0.2 mol L^{-1}) was slowly added to adjust the pH to approximately 9. The resulting mixture was aged in a water bath at 80 °C for 2 h. The precipitate was collected by centrifugation, washed thoroughly with deionized water, and dried in an oven at 80 °C for 12 h. The dried powders were then ground and calcined in a muffle furnace, heating from room temperature to 300 °C at a ramp rate of 2 °C min^{-1}, and maintained at 300 °C for 2 h. For references, Au/TiO_2-A, Au/TiO_2-P25, and Au/TiO_2-R were synthesized using the identical preparation method as Au/TiO_2. TiO_2-supported Pd, Pt, and Cu catalysts were prepared using the same synthesis method as Au/TiO_2 for comparison.

Fe/ZSM-5 was prepared using the ball milling method. In a typical procedure, 10.0 g of NH_4-ZSM-5 and 0.48 g of $FeCl_3 \cdot 6H_2O$ were placed in hardened steel jars, and ball milling was conducted at 800 rpm at room temperature for 30 min using a planetary ball mill (Retsch GmbH, Emax). The resulting powders were calcined in a muffle furnace, with the temperature increased from room temperature to 400 °C at a rate of 2 °C min^{-1}, and held at 400 °C for 4 h.

2.2. Catalyst Characterization

The inductively coupled plasma-atomic emission spectroscopy (ICP-AES) (710-ES, Varian, Palo Alto, CA, USA) determined the actual metal loadings of Au and Fe. X-ray diffraction (XRD) patterns were recorded by using a Philips X'Pert Pro Super diffractometer (Malvern Panalytical, Almelo, The Netherlands) with Cu-Kα radiation (λ = 1.54178 Å). Aberration-corrected high-angle annular dark field scanning transmission electron microscopy (HAADF-STEM) images were carried out on a JEOL ARM-200F (JEOL Ltd., Tokyo, Japan) operating at an accelerating voltage of 200 kV. XPS measurements were conducted on an X-ray photoelectron spectrometer (VG ESCALAB MK II, Thermo Fisher Scientific, Waltham, MA, USA) with Mg Kα = 1253.6 eV as the exciting source. Ultraviolet-visible (UV-Vis) spectroscopy spectra were recorded on a Shimadazu Solid 3700 DUV (Shimadzu, Kyoto, Japan). The X-ray absorption spectroscopy (XAS) measurements were carried out at the BL11B beamline of the Shanghai Synchrotron Radiation Facility (SSRF, Shanghai Institute of Applied Physics, Chinese Academy of Sciences, Shanghai 201204, China) in the fluorescence mode (https://cstr.cn/31124.02.SSRF.BL11B (accessed on 6 October 2023)).

Fluorescence emission spectroscopy was used to detect hydroxyl radical (·OH), employing terephthalic acid as a probe molecule. Terephthalic acid readily reacts with ·OH radicals to form the highly fluorescent 2-hydroxyterephthalic acid. For this analysis, a fixed amount of terephthalic acid was dissolved in 2×10^{-3} mol L^{-1} NaOH to prepare a 5×10^{-4} mol L^{-1} terephthalic acid solution. The terephthalic acid solution was used instead of

H_2O to disperse the catalyst. After the reaction at 30 °C for 2 h and the removal of solid catalyst, the liquid solution was subjected to fluorescence spectroscopy measurements. The spectrum was recorded on a Horiba Fluorolog-3-Tau and deltaflex fluorescence spectrophotometer with an excitation wavelength of 315 nm.

High resolution mass spectrometry (HRMS) measurement was conducted on a LTQ-Orbitrap XL using the ESI technique. The reaction was conducted over 150 mg of Au/TiO_2 + Fe/ZSM-5 with mechanical stirring (1000 rpm) in 15 mL of H_2O under 15 bar of CH_4, 40 bar of CO, and 6 bar of O_2 at 30 °C for 2 h. During the reaction, 100 mg of TEMPO was added into the reaction solution. Following the completion of the reaction, the mixture was promptly centrifuged and used for further HRMS measurement.

In situ diffuse reflectance Fourier transform spectroscopy (DRIFTS) measurement was conducted in a cell with a Fourier transform infrared spectrometer (TENSOR II Sample Compartment) and a liquid nitrogen-cooled detector. The catalyst was pretreated by 1 bar of argon (30 mL min^{-1}) at 150 °C for 30 min, followed by cooling to 30 °C, the background spectra of the sample were acquired. For all DRIFTS measurements, the test temperature was maintained at 30 °C. This temperature has been explicitly noted for each individual adsorption measurement. For CH_4, CO, O_2, and H_2O co-adsorption, 10 mg of Au/TiO_2 and 20 mg of Fe/ZSM-5 were used for measurement. 80% CH_4 (CO as a balanced gas, 15 mL min^{-1}) and 20% O_2 (argon as a balanced gas, 15 mL min^{-1}) were used as the co-fed gases. For CH_4, CO, H_2O_2, and H_2O co-adsorption, 30 mg of Fe/ZSM-5 was used for measurement. 80% CH_4 (CO as a balanced gas, 15 mL min^{-1}) and argon (15 mL min^{-1}) were used as the reactant gaseous. H_2O_2 solution was brought into the chamber by co-fed gases.

Synchrotron vacuum ultraviolet photoionization mass spectrometry (SVUV-PIMS) measurements were conducted at the combustion beamline (BL03U) of the National Synchrotron Radiation Laboratory (Hefei, China). In each experiment, 100 mg of 20–40 mesh catalyst (or quartz for blank tests) was loaded into a quartz reactor fitted with a ~0.1 mm nozzle. The Au/TiO_2 and Fe/ZSM-5 mass ratio was fixed at 1:2. The reactor was coupled to an online SVUV-PIMS spectrometer, and the gas flow was switched to the reaction mixture (15 mL min^{-1} of CH_4, 40 mL min^{-1} of CO, and 6 mL min^{-1} of O_2), water was introduced by the feed gas. Data were acquired at 30 °C in 600 s intervals (200 s sampling time) under constant 11.5 eV photon energy and 2 Torr pressure.

2.3. Catalyst Performance Test

Methane oxidation reactions with O_2 as an oxidant in the presence of CO were carried out in a 50-mL Hastelloy slurry reactor (Shanghai Yanzheng Experiment Instrument Co., LTD, Shanghai, China). In a typical process, the reaction was conducted over 50 mg of Au/TiO_2 and 100 mg of Fe/ZSM-5 (denoted as Au/TiO_2 + Fe/ZSM-5) with mechanical stirring (1000 rpm) in 15 mL of H_2O under 15 bar of CH_4, 40 bar of CO, and 6 bar of O_2 at 30 °C for 6 h. After the reaction, the autoclave was cooled down to below 10 °C and filtered to remove the catalyst before analyses. Unless otherwise specified, 150 mg of Au/TiO_2 + Fe/ZSM-5 refers to a combination of 50 mg of Au/TiO_2 and 100 mg of Fe/ZSM-5.

Liquid products were analyzed by ^1H nuclear magnetic resonance (^1H-NMR). 66.7 μL of DMF was introduced into 100 mL of D_2O as an internal standard solution. 100 μL of the internal standard solution and 600 μL of the reaction sample were added into NMR tubes for measurement. The signal of protons from the solvent H_2O is much stronger than that from the products. Therefore, all ^1H NMR spectra were recorded using a pre-saturation solvent suppression technique to suppress the dominant H_2O signal. The amount of $HOCH_2OH$ was quantified via the acetylacetone color-development method (UV-Vis spectrophotometer, Cary 60 UV-Vis, Agilent, Santa Clara, CA, USA). In this work, CH_3OH, $HOCH_2OH$, and HCOOH originated from CH_4, while CH_3COOH was sourced from both CH_4 and CO. Therefore, we calculated the product yield (micromoles of acetic acid per gram of the catalyst, μmol g_{cat}^{-1}) and CH_3COOH selectivity (%, in liquid) on a molecule basis using Equations (1) and (2).

$$\text{Products yield } (\mu\text{mol } g_{cat}^{-1}) = \frac{n_{product}}{g_{cat}} \quad (1)$$

$$CH_3COOH \text{ selectivity } (\%) = \frac{n_{CH_3COOH}}{n_{product}} \times 100\% \quad (2)$$

In Equation (1), $n_{product}$ represented the total moles of liquid products, g_{cat} was the mass of the catalysts. In Equation (2), n_{CH_3COOH} was the mole of produced CH_3COOH.

Elevated-pressure operation requires specialized equipment and strict CO safety protocols. Although high pressure increases cost, it is common in industry. Ongoing catalyst optimization aims to improve CO utilization and reduce required pressure while maintaining performance for practical application.

An H_2O_2 synthesis experiment was carried out in a 50-mL Hastelloy slurry reactor. 15 mg of catalyst was added into the reaction reactor with 15 mL of H_2O. The reaction was conducted with mechanical stirring (1000 rpm) under

40 bar of CO, 6 bar of O_2, and 15 bar of N_2 at 30 °C for 1 h. After completion of the reaction, 1 mL of the sample was combined with 20 mL of H_2O and 10 mL of 3 mol L^{-1} sulfuric acid in a titration vessel. Subsequently, 20 μL of Ferroin solution was added to the mixture under continuous stirring. The resulting solution was then gradually titrated with 0.002 mol L^{-1} $Ce(SO_4)_2$ solution until a persistent pale blue endpoint was observed.

For methane oxidation with H_2O_2 in the presence of CO, the experiments were conducted in a 50-mL Hastelloy slurry reactor. The reactor contained 15 mg of catalyst, 15 mL of H_2O containing 1500 μmol of H_2O_2. The reaction was conducted with mechanical stirring (1000 rpm) under 15 bar of CH_4, 40 bar of CO, and 6 bar of N_2 at 30 °C for 1 h.

H_2O_2 decomposition experiment was carried out in a 50-mL Hastelloy slurry reactor. 15 mg of catalyst was added into the reaction reactor with 15 mL of H_2O containing 1500 μmol of H_2O_2. The reaction was conducted with mechanical stirring (1000 rpm) under 40 bar of CO and 21 bar of N_2 at 30 °C for various time. After completion of the reaction, 1 mL of the sample was combined with 20 mL of H_2O and 10 mL of 3 mol L^{-1} sulfuric acid in a titration vessel. Subsequently, 20 μL of Ferroin solution was added to the mixture under continuous stirring. The resulting solution was then gradually titrated with 0.002 mol L^{-1} $Ce(SO_4)_2$ solution until a persistent pale blue endpoint was observed.

To trace the fate of carbon atoms from CH_4 and CO, ^{13}C labeled CH_4 ($^{13}CH_4$) with 99% natural abundance was used in the coreaction with CO and O_2. The reaction was conducted over 150 mg of Au/TiO_2 + Fe/ZSM-5 with mechanical stirring (1000 rpm) in 15 mL of H_2O under 8 bar of $^{13}CH_4$, 8 bar of CO, and 4 bar of O_2 at 30 °C for 6 h. ^{13}C labeled CO (^{13}CO) with 99% natural abundance was used in the coreaction with CH_4 and O_2. The reaction was conducted over 150 mg of Au/TiO_2 + Fe/ZSM-5 with mechanical stirring (1000 rpm) in 15 mL of H_2O under 8 bar of CH_4, 8 bar of ^{13}CO, and 4 bar of O_2 at 30 °C for 6 h.

3. Results and Discussion

3.1. Design, Synthesis, and Characterization of the Catalysts

Au/TiO_2 was synthesized via hydrothermal treatment followed by deposition-precipitation processing. The content of Au in Au/TiO_2 was 1.7 wt%, as determined by inductively coupled plasma atomic emission spectroscopy (ICP-AES) (Table S1). X-ray diffraction (XRD) analysis showed that no detectable metallic Au or Au oxide in Au/TiO_2 (Figure S1). As references, Au/TiO_2-A, Au/TiO_2-P25, Au/TiO_2-R (1.6~1.7 wt% Au) prepared using the identical preparation method as Au/TiO_2 (Table S1). Aberration-corrected high-angle annular dark field scanning transmission electron microscopy (HAADF-STEM) confirmed the presence of Au nanoparticles in Au/TiO_2 with an average size of 5.7 nm (Figure 1a). The homogeneous distribution of Au species was further corroborated by energy-dispersive X-ray spectroscopy (EDS) mapping results (Figure 1b). The lattice spacing of the Au nanoparticles was measured at 0.24 nm, corresponding to (111) face-centered cubic (fcc) Au (Figure 1c) [26,27]. In addition, TEM analyses revealed that Au formed relatively large nanoparticles on Au/TiO_2-A, Au/TiO_2-P25, and Au/TiO_2-R (Figure S2). For all samples, the peaks observed at approximately 83.1 eV and 86.9 eV correspond to the Au $4f_{7/2}$ and Au $4f_{5/2}$ binding energies of Au^0 (Figure S3) [28–30], respectively.

To synthesize Fe/ZSM-5 catalyst, we adopted a ball-milling approach, while preparing Fe/ZSM-5-imp via conventional incipient wetness impregnation for comparative studies. XRD analysis revealed no detectable peaks attributable to crystalline Fe or Fe oxide phases in Fe/ZSM-5 (Figure S4). HAADF-STEM images of Fe/ZSM-5 showed the presence of atomically dispersed Fe species, as highlighted by yellow cycles (Figure 1d). The EDS mapping results further confirmed the homogeneous distribution of Fe species (Figure 1e). In contrast, Fe/ZSM-5-imp exhibited coexistence of atomically dispersed Fe species and FeO_x nanoparticles (Figure S5). XPS analysis reveals binding energies at 711.0 eV and 724.6 eV for Fe/ZSM-5, which are characteristic of Fe^{3+} species [31–33]. The corresponding peaks for Fe/ZSM-5-imp appeared at lower binding energies of 710.8 eV and 724.4 eV, respectively (Figure S6). This shift to lower binding energies indicates that the Fe species in Fe/ZSM-5-imp possessed a lower average oxidation state compared to those in Fe/ZSM-5. Ultraviolet-visible spectroscopy (UV-Vis) analysis revealed trace Fe impurities (<0.03 wt%) in ZSM-5 as monomeric tetrahedral (MT) and octahedral (MO) Fe^{3+} (Figure 1f) [34–36]. Fe incorporation (1 wt%) intensified these signals and introduced polynuclear clusters (360 nm) and Fe_2O_3 nanoparticles (>450 nm). Deconvolution showed ball-milled Fe/ZSM-5 retained 62.7% monomeric Fe versus 41.3% in impregnated Fe/ZSM-5-imp (41.2% Fe_2O_3) (Table S2), confirming superior Fe dispersion in ball-milled Fe/ZSM-5, consistent with HAADF-STEM results.

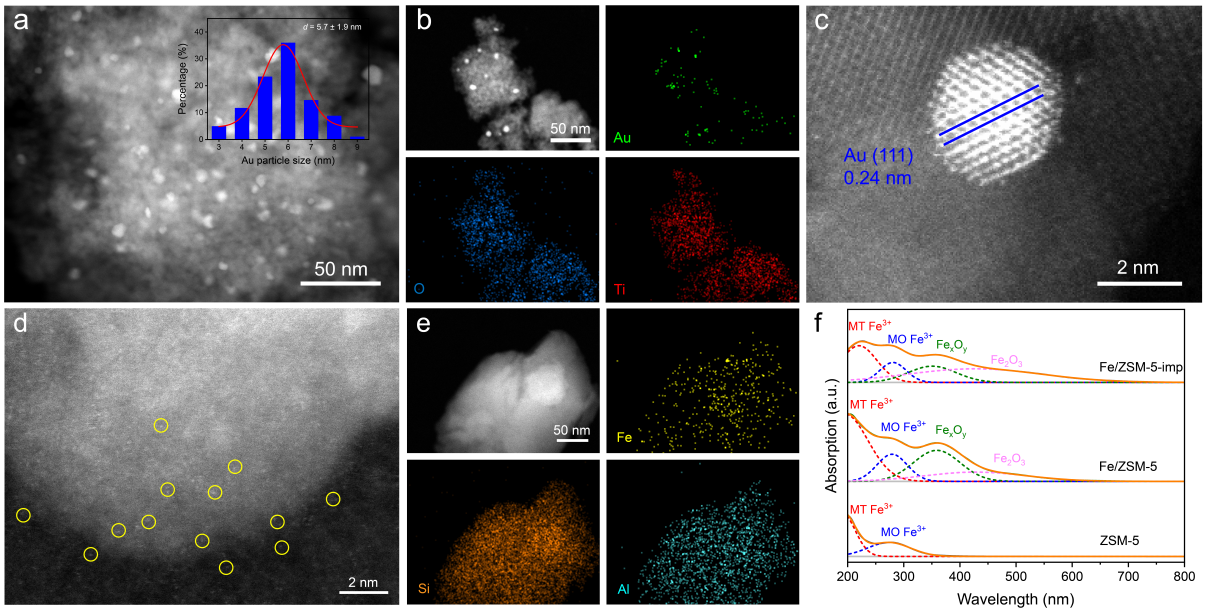

Figure 1. Identification of the active sites. (**a**) Aberration corrected HAADF-STEM image and particle size distribution of Au nanoparticles. (**b**) and (**c**) EDS mapping images and HAADF-STEM image of Au/TiO_2. (**d**) and (**e**) HAADF-STEM image and corresponding EDS mapping images. (**f**) UV-Vis spectral profiles of ZSM-5, Fe/ZSM-5, and Fe/ZSM-5-imp samples.

To further study the chemical state and coordinated environmental of Fe in the Fe-containing samples. X-ray absorption near edge spectroscopy (XANES) showed that the absorption edge of Fe/ZSM-5 was shifted to higher energy relative to Fe foil and closely resembled that of Fe_2O_3 (Figure S7a). A pre-edge feature at 7114 eV, characteristic of the $1s \rightarrow 3d$ transition of Fe^{3+} in tetrahedral or distorted octahedral coordination, further indicated that Fe predominantly existed as Fe^{3+} species [37]. The Fourier-transformed k^3-weighted extended X-ray absorption fine structure (EXAFS) spectrum of Fe/ZSM-5 exhibited a dominant peak at ~1.6 Å, corresponding to the Fe-O first shell, and a weak peak at ~2.6 Å assigned to the Fe-Fe second shell (Figure S7b) [38]. Notably, no distinct Fe-Fe first-shell scattering was observed, in contrast to Fe foil. EXAFS fitting yielded an Fe-O coordination number (*CN*) of 5.3 ± 0.3 with a bond length of 2.04 ± 0.01 Å and an Fe-Fe *CN* of only 0.4 ± 0.7 at 3.06 ± 0.13 Å (Table S3), confirming the atomic dispersion of Fe species in Fe/ZSM-5. By comparison, Fe/ZSM-5-imp exhibited a substantially higher Fe-Fe *CN* of 1.7 ± 0.6 with a bond length of 3.03 ± 0.06 Å, indicative of the formation of large FeO_x particles.

3.2. Optimization of Tandem Catalysis Enables Methane Oxidation to Acetic Acid

Building on insights into H_2O_2 synthesis and acetic acid formation, we developed a tandem route for methane conversion by integrating Au/TiO_2 and Fe/ZSM-5 (Figure 2a). H_2O_2 forms on Au/TiO_2 and subsequently migrates to Fe/ZSM-5 for methane oxidation to acetic acid [15,23]. To validate the effectiveness of tandem catalytic mechanism, we first examined H_2O_2 synthesis, confirming CO is essential, as O_2 and H_2O alone produced no H_2O_2 over Au/TiO_2 or Fe/ZSM-5. Au/TiO_2 catalysts screened for H_2O_2 synthesis from CO/O_2/H_2O via colorimetry. Among these catalysts, Au/TiO_2 exhibited the highest H_2O_2 production (2600 μmol g_{cat}^{-1}), outperforming Au/TiO_2-A (2200 μmol g_{cat}^{-1}), Au/TiO_2-P25 (1600 μmol g_{cat}^{-1}), and Au/TiO_2-R (100 μmol g_{cat}^{-1}) (Figure 2b), highlighting that optimal Au dispersion and electronic structure enhance catalytic activity. In contrast, Fe/ZSM-5 produced a low H_2O_2 yield of 30 μmol g_{cat}^{-1} (Figure S8).

We then screened catalysts for methane oxidation with H_2O_2 in the presence of CO over Fe species on ZSM-5 supports, ^{1}H nuclear magnetic resonance (NMR) and UV-Vis were employed to quantify the liquid products (Figures S9 and S10). We found that ball-milled Fe/ZSM-5 (predominantly featuring isolated Fe sites) significantly enhances the yield of acetic acid, reaching 817.6 μmol g_{cat}^{-1} (Figure 2c). In contrast, although Fe/ZSM-5-imp (containing more FeO_x particles) exhibited a slightly higher selectivity towards acetic acid (93.6% vs. 86.2%), its total oxygenate yield was markedly lower (610.2 μmol g_{cat}^{-1} vs. 948.5 μmol g_{cat}^{-1}). Consequently, its acetic acid yield (571.1 μmol g_{cat}^{-1}) was actually lower than that achieved over the Fe/ZSM-5. These results demonstrated that isolated Fe sites are more effective than FeO_x particles in promoting the conversion of CH_4 to oxygenates, particularly in enhancing acetic acid yield. The presence of FeO_x particles may be associated with

lower overall catalytic activity, thereby limiting the actual production of acetic acid. Conversely, no liquid products were detected for Au/TiO_2 (Figure S11). Collectively, the structurally optimized Au/TiO_2 and Fe/ZSM-5 were selected for spatial coupling due to peak catalytic performance. Based on above-mentioned findings, we performed methane oxidation with O_2 in the presence of CO in H_2O solvent. The standard reaction was conducted over 150 mg of catalyst with mechanical stirring (1000 rpm) in 15 mL of H_2O under 15 bar of CH_4, 40 bar of CO, and 6 bar of O_2 at 30 °C for 6 h. Neither Au/TiO_2 nor Fe/ZSM-5 alone produced detectable oxygenates. To clarify this, CH_4 oxidation was examined over Au/TiO_2 with varying H_2O_2 dosages. Despite minimal residual H_2O_2 after reaction, no liquid oxygenates were detected (Figure S12), suggesting rapid, nonproductive H_2O_2 decomposition to H_2O and O_2, which prevents oxygenate accumulation.

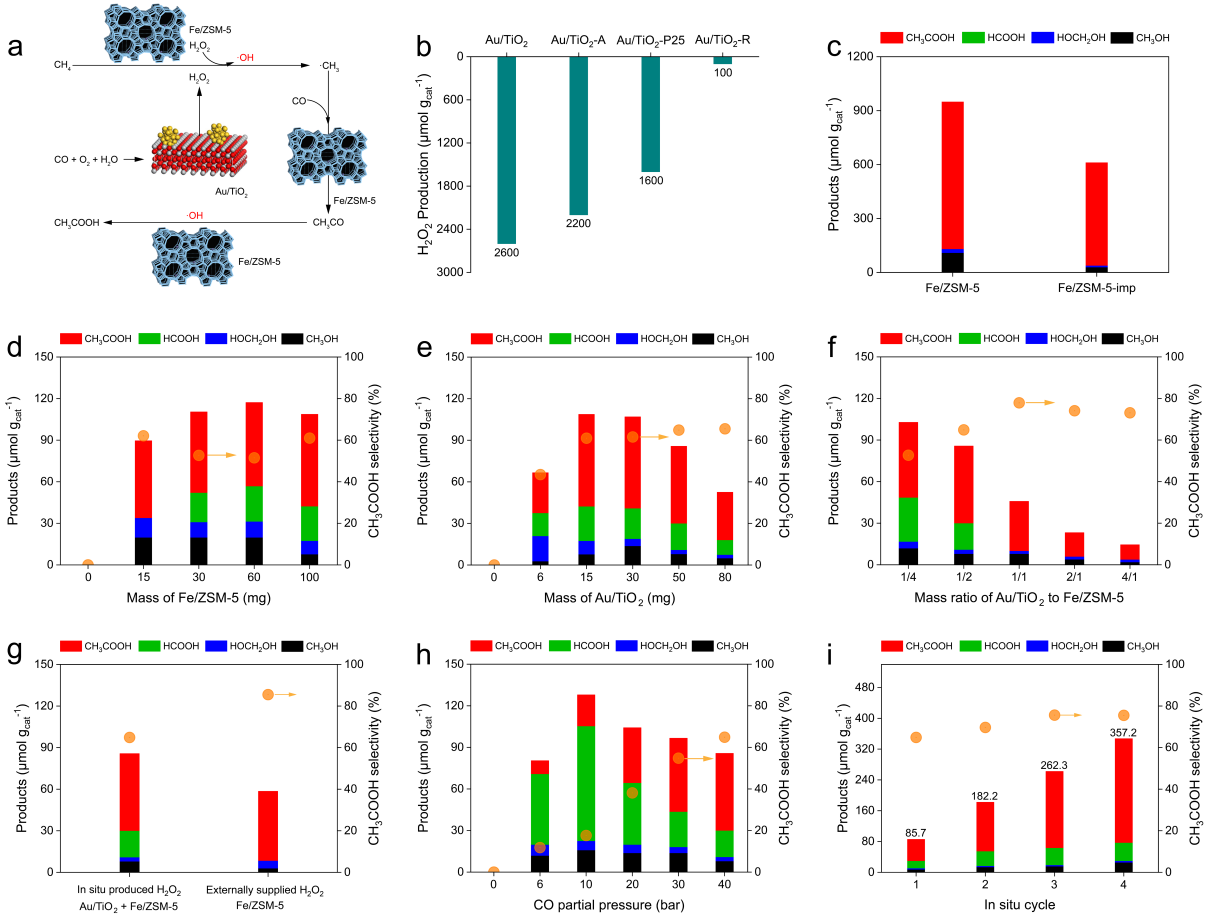

Figure 2. Tandem catalysis enables methane oxidation to acetic acid. (**a**) Concept for acetic acid synthesis from $CH_4 + CO + O_2 + H_2O$ system. (**b**) H_2O_2 synthesis from the reaction of $CO + O_2 + H_2O$. The reaction was conducted over 15 mg of catalyst with mechanical stirring (1000 rpm) in 15 mL of H_2O under 15 bar of N_2, 40 bar of CO, and 6 bar of O_2 at 30 °C for 1 h. (**c**) Acetic acid synthesis from the reaction of $CH_4 + CO + H_2O_2$. The reaction was conducted over 15 mg of catalyst with mechanical stirring (1000 rpm) in 15 mL of H_2O containing 1500 μmol of H_2O_2 under 15 bar of CH_4, 40 bar of CO, and 6 bar of N_2 at 30 °C for 1 h. (**d**–**i**) Acetic acid synthesis from $CH_4 + CO + O_2 + H_2O$ system by verifying (**d**) Fe/ZSM-5 loading, (**e**) Au/TiO_2 loading, (**f**) Mass ratio of the Au/TiO_2 to Fe/ZSM-5. The standard reaction was conducted over 150 mg of catalyst with mechanical stirring (1000 rpm) in 15 mL of H_2O under 15 bar of CH_4, 40 bar of CO, and 6 bar of O_2 at 30 °C for 6 h. (**g**) Methane oxidation with *in situ* produced H_2O_2/externally supplied H_2O_2 in the presence of CO. For externally supplied H_2O_2, the reaction was conducted over 100 mg of the Fe/ZSM-5 with mechanical stirring (1000 rpm) in 15 mL of H_2O containing 234 μmol of H_2O_2 under 15 bar of CH_4, 40 bar of CO, and 6 bar of N_2 at 30 °C for 6 h. (**h**) CO partial pressure-dependent product yields over Au/TiO_2 + Fe/ZSM-5 under standard conditions. CO dependent catalytic performance under standard reaction conditions. (**i**) *In situ* cycle test under standard reaction conditions.

To further explored how the mass ratio of Au/TiO_2 to Fe/ZSM-5 influenced the catalytic performance. We firstly optimized the Fe/ZSM-5 content while maintaining a fixed Au/TiO_2 loading of 15 mg. As shown in Figure 2d, no oxygenated products were detected in the absence of Fe/ZSM-5. Increasing the Fe/ZSM-5 mass from 15 to 100 mg resulted in oxygenate yields ranging from 89.6 to 117.2 μmol g_{cat}^{-1}, with acetic acid selectivity between 62.1%

and 51.5% (Table S4). Based on these results, 100 mg of Fe/ZSM-5 was selected for further optimization. Subsequent tests with fixed Fe/ZSM-5 (100 mg) and varying Au/TiO_2 loadings revealed that oxygenate formation required Au/TiO_2, with the highest yield (108.7 μmol g_{cat}^{-1}) and acetic acid selectivity (61.0%) achieved at 15 mg of Au/TiO_2 (Figure 2e and Table S5). While higher Au/TiO_2 mass loadings (50~80 mg) improved acetic acid selectivity (up to 65.5%), the oxygenate yield dropped significantly (52.5 μmol g_{cat}^{-1} at 80 mg), prompting the selection of 50 mg of Au/TiO_2 for balance. Further investigations at a total catalyst mass of 150 mg demonstrated that increasing the mass ratio of Au/TiO_2 to Fe/ZSM-5 ranging from 1/4 to 4/1 sharply reduced oxygenate yields from 102.8 to 14.5 μmol g_{cat}^{-1} but enhanced acetic acid selectivity from 52.7% to 77.9%, which plateaued at higher ratios (Figure 2f and Table S6). Physically mixing 50 mg of Au/TiO_2 and 100 mg of Fe/ZSM-5 (denoted as Au/TiO_2 + Fe/ZSM-5) yielded 85.7 μmol g_{cat}^{-1} of liquid products, with the CH_3COOH selectivity up to 64.9%, corresponding to the CH_3COOH yield of 55.6 μmol g_{cat}^{-1}.

To provide a more quantitative comparison between methane oxidation using externally supplied H_2O_2 and *in situ* generated H_2O_2, we evaluated the performance of externally supplied H_2O_2 versus *in situ* generated H_2O_2 in methane oxidative coupling to acetic acid. The results revealed that the *in situ* H_2O_2 pathway achieved a higher oxygenate yield (85.7 μmol g_{cat}^{-1}) compared to the external H_2O_2 route (58.5 μmol g_{cat}^{-1}), despite the higher acetic acid (85.5%) for externally supplied H_2O_2 system (Figure 2g). These results supporting the intrinsic advantage of tandem catalysis in enhancing H_2O_2 utilization efficiency due to its proximity-driven delivery between Au/TiO_2 and Fe/ZSM-5, which aligns with our conclusion that spatially confined *in situ* H_2O_2 generation favors overall oxygenate production despite the selectivity trade-offs. Importantly, our current work represents a significant advance by enabling methane-to-acetic acid conversion at 30 °C using O_2 as the terminal oxidant in the presence of CO, whereas previous systems required both externally supplied H_2O_2 or elevated temperatures (Table S7). We then calculated the Fe-based turnover frequency (TOF) values, it was found that our tandem catalytic system exhibits TOF values ranging from 0.08 to 0.58 h^{-1} at low temperatures (30 to 60 °C). These values outperform those reported for Rh-Fe/MoS_2 (0.05 h^{-1} at 25 °C and 0.18 h^{-1} at 80 °C) and Au-Fe/ZSM-5 (0.41 h^{-1} at 60 °C), indicating enhanced low-temperature performance of tandem catalyst when using O_2 in the presence of CO, although its performance remains inferior to systems utilizing externally added H_2O_2. We prepared Pd/TiO_2, Pt/TiO_2, and Cu/TiO_2 using the same method as Au/TiO_2 for comparison. Under identical conditions, the physical mixture of Au/TiO_2 and Fe/ZSM-5 showed the best performance (85.7 μmol g_{cat}^{-1}), far exceeding Pd/TiO_2 (10.0 μmol g_{cat}^{-1}), while Pt/TiO_2 and Cu/TiO_2 exhibited no activity in this tandem system (Figure S13a). H_2O_2 measurements after reaction further show that Au is the most effective catalyst for H_2O_2 generation (Figure S13b), leading to higher local H_2O_2 concentration and thus improved methane oxidation to oxygenates.

Considering both yield and selectivity, a 1:2 mass ratio of Au/TiO_2 to Fe/ZSM-5 was used. No liquid products formed without CO. Increasing CO to 6 bar produced 80.4 μmol g_{cat}^{-1}, mainly HCOOH (63.4% selectivity). The maximum yield of 127.9 μmol g_{cat}^{-1} with 17.6% CH_3COOH selectivity occurred at 10 bar, while further increasing CO to 40 bar reduced the yield to 85.7 μmol g_{cat}^{-1} (Figure 2h and Table S8), likely due to active-site blockage [13,39]. However, the selectivity towards CH_3COOH increased significantly from 17.6% to 64.9%, indicating that higher CO partial pressures promoted the formation of CH_3COOH.

We further examined the effect of methane partial pressure on the performance of Au/TiO_2 + Fe/ZSM-5. Increasing the CH_4 pressure from 3 to 15 bar raised the product yield from 13.3 to 85.7 μmol g_{cat}^{-1} (Figure S14 and Table S9), while CH_3COOH selectivity decreased from 83.5% to 64.9%. At low CH_4 pressure, abundant CO mainly promotes O_2 activation and favors CH_3COOH formation via methyl-CO coupling. As CH_4 pressure increases, more CO is consumed to generate reactive oxygen species for oxidizing additional methyl intermediates. This promotes competing pathways, including direct oxidation to C_1 products and methyl-CO coupling. Consequently, although CH_3COOH formation continues, the increased production of C_1 products lowers its selectivity, reflecting the balance between coupling and oxidation pathways. The time-dependent catalytic activity of Au/TiO_2 + Fe/ZSM-5 demonstrated a continuous increase in liquid products yield with reaction time, while the total oxygenates yield increased continuously with reaction time, the selectivity for CH_3COOH declined from 82.6% to 64.9% (Figure S15 and Table S10). We attribute this primarily to accumulation of in-situ generated H_2O_2 during extended reactions. Elevated H_2O_2 concentrations promote key side pathways, notably enhanced formation of C_1 oxygenates including CH_3OH, $HOCH_2OH$, and HCOOH.

We evaluated catalyst stability using an *in situ* recycling approach. Oxygenate yields increased over four cycles to 85.7, 182.8, 262.3, and 357.2 μmol g_{cat}^{-1} (Figure 2i), corresponding to cumulative yields 2.1, 3.1, and 4.2 times higher than the first cycle. Meanwhile, acetic acid selectivity among oxygenates increased from 64.9% to 75.5%. TEM images of the physically mixed catalyst after four cycles showed an average Au particle size of 5.7 ± 1.2 nm, nearly identical to the fresh catalyst (5.7 ± 1.9 nm) (Figure S16a,b). XPS analysis further confirmed that the valence states of Au and Fe remained essentially unchanged (Figure S16c,d), demonstrating excellent

catalyst stability. The extremely low leaching (<0.01% for both metals) under mild conditions (30 °C) rules out significant cross-contamination between catalyst components (Table S11).

3.3. Mechanism Studies Towards Methane Oxidation by Tandem Catalysis

Isotopic labeling experiments were conducted to identify the carbon source of the oxygenates using $^{13}CH_4 + CO + O_2$ and $CH_4 + {}^{13}CO + O_2$ in H_2O. With $^{13}CH_4$, ^{13}C NMR signals at −4.91, 20.47, 48.92, 81.85, and 166.98 ppm corresponded to $^{13}CH_4$, $^{13}CH_3COOH$, $^{13}CH_3OH$, $HO^{13}CH_2OH$, and $H^{13}COOH$ (Figure 3a) [40,41], while ^1H NMR showed their characteristic satellite peaks (Figure S17) [42]. Using ^{13}CO, only $^{13}CO_2$ and $CH_3{}^{13}COOH$ signals appeared [43], with no $^{13}CH_3OH$ or $H^{13}COOH$ detected [44]. These results confirm that CH_4 provides the carbon for oxygenates, with CH_4 and CO supplying the methyl and carbonyl groups, respectively, for CH_3COOH formation.

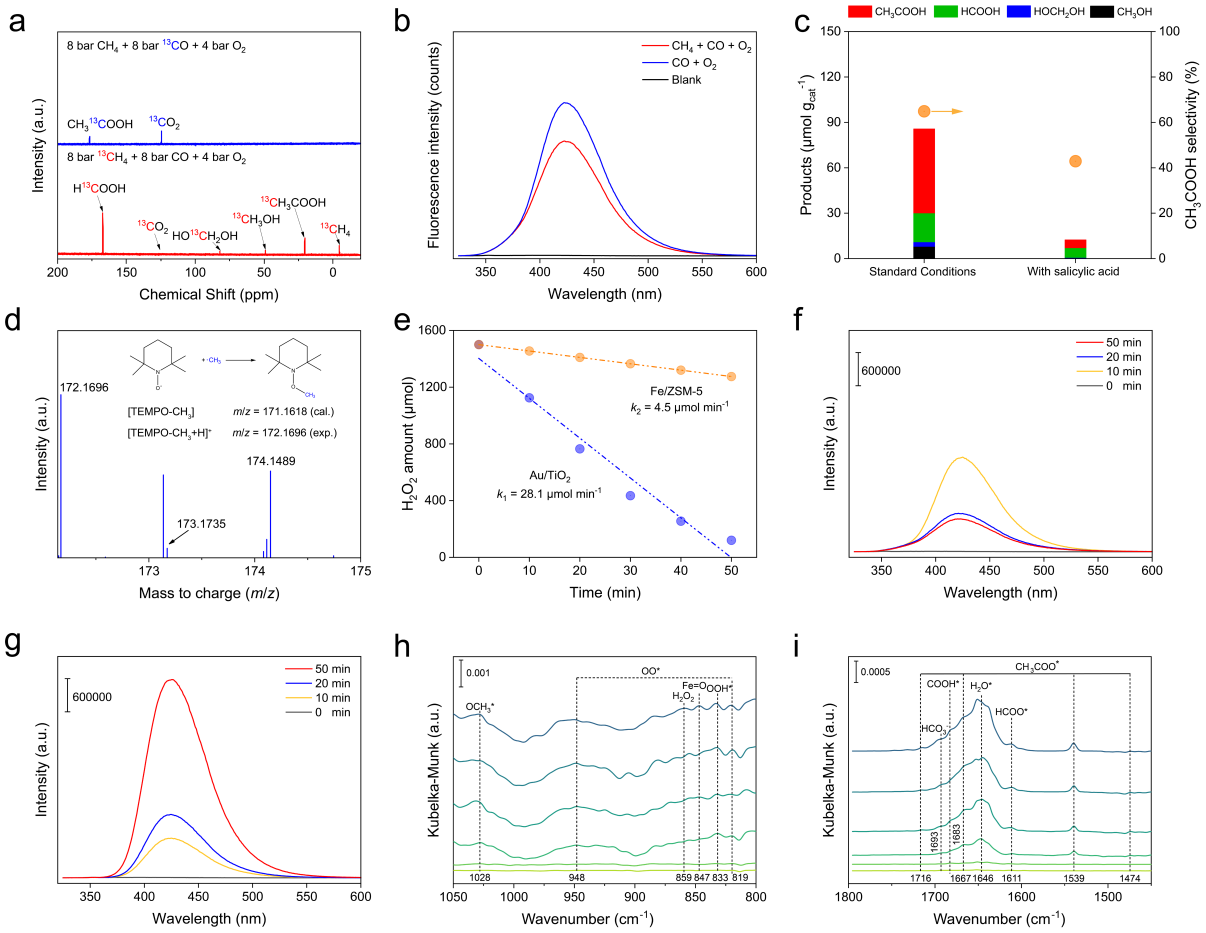

Figure 3. Reaction mechanism studies. (**a**) ^{13}C NMR spectrum. The reaction was conducted over 150 mg of Au/TiO_2 + Fe/ZSM-5 with mechanical stirring (1000 rpm) in 15 mL of H_2O under 8 bar of CH_4 (or 8 bar of $^{13}CH_4$), 8 bar of CO (or 8 bar of ^{13}CO), and 4 bar of O_2 at 30 °C for 6 h. (**b**) Fluorescence emission spectra. The reaction was conducted under standard reaction conditions except for 15 mL of NaOH-terephthalic acid solution added. (**c**) Quenching experiment. The reaction was conducted over 150 mg of Au/TiO_2 + Fe/ZSM-5 with mechanical stirring (1000 rpm) in 15 mL of H_2O under 15 bar of CH_4, 40 bar of CO, and 6 bar of O_2 at 30 °C for 6 h. 1 mmol of salicylic acid as the scavenger. (**d**) HRMS spectra for TEMPO-trapped methyl radicals and hydroxyl radicals. The reaction was conducted under standard reaction conditions except for 100 mg of TEMPO added. (**e**) H_2O_2 decomposition experiments. (**f** and **g**) Fluorescence emission spectra over Au/TiO_2 and Fe/ZSM-5. The reaction was conducted over 15 mg of catalyst with mechanical stirring (1000 rpm) in 15 mL of H_2O containing 1500 μmol H_2O_2 under 21 bar of N_2 and 40 bar of CO at 30 °C for different reaction time. (**h** and **i**) *In-situ* DRIFTS spectra of Au/TiO_2 + Fe/ZSM-5 at different wavenumber intervals after the exposure to CH_4, CO, O_2, and H_2O at 30 °C for 15 min (0 to 15 min, from bottom to top).

To probe the role of hydroxyl radicals, fluorescence spectroscopy was performed [45,46]. The ·OH signal in the $CO/O_2/H_2O$ system was stronger than in the $CH_4/CO/O_2/H_2O$ mixture (Figure 3b), indicating ·OH participation

in methane oxidation. Quenching experiments using salicylic acid further confirmed this role: the total oxygenate yield decreased from 85.7 to 12.3 μmol g_{cat}^{-1}, with acetic acid selectivity dropping from 64.9% to 42.9% (Figure 3c). High-resolution mass spectrometry with 2,2,6,6-tetramethylpiperidine-1-oxyl (TEMPO) as a trapping agent detected TEMPO-CH_3 ([TEMPO-CH_3+H]$^+$, *m*/*z* 172.1696) and TEMPO-OH ([TEMPO-OH+H]$^+$, *m*/*z* 174.1489) (Figure 3d) [15,36]. These results confirm a free-radical pathway, where ·OH radicals play a key role in methane activation and oxygenate formation. To investigate ·OH formation over Au/TiO_2 and Fe/ZSM-5, H_2O_2 decomposition experiments were conducted to clarify their roles. Au/TiO_2 showed high H_2O_2 decomposition activity (28.1 μmol min^{-1}, Figure 3e), but fluorescence measurements revealed non-linear ·OH generation (Figure 3f), indicating mainly non-productive decomposition to H_2O and O_2. In contrast, Fe/ZSM-5 displayed lower H_2O_2 decomposition activity (4.5 μmol min^{-1}) yet enabled sustained ·OH accumulation (Figure 3g), suggesting efficient H_2O_2 activation. These results highlight the complementary roles of the two components. Au/TiO_2 efficiently produces H_2O_2, whereas Fe/ZSM-5 activates it to generate reactive ·OH radicals, thereby explaining their synergistic cooperation.

To evaluate the role of water, we examined pH effects on catalytic performance. Under acidic conditions (HNO_3), the oxygenate yield increased from 85.7 to 105.1 μmol g_{cat}^{-1} at pH = 3, while acetic acid selectivity remained at 64.9%, likely due to enhanced O_2 protonation and H_2O_2 formation (Figure S18). Under alkaline conditions (NaOH, pH~11), the yield further increased to 226.2 μmol g_{cat}^{-1}, but acetic acid selectivity decreased to 47.7%, indicating a shift toward C1 products favored by base-mediated pathways. Control experiments replacing H_2O with cyclohexane or acetonitrile gave no oxygenates (Figure S19), confirming that water is essential as both solvent and reactant. Mechanistically, H_2O participates in a water-gas shift reaction with CO to form COOH* and H*, where H* promotes O_2 protonation to generate H_2O_2 as the key oxidant. Thus, water plays a dual role as reaction medium and stabilizer.

To identify key intermediates, *in situ* diffuse reflectance infrared Fourier transform spectroscopy (DRIFTS) measurement was performed on a physical mixture of Au/TiO_2 and Fe/ZSM-5 exposed to CH_4, CO, O_2, and H_2O (1 bar, 30 °C, 15 min). Peaks at 948 and 819 cm^{-1} correspond to M-OO* and M-OO-M* species (Figure 3h), indicating O_2 activation [47]. Signals at 859 cm^{-1} (free H_2O_2) and 833 cm^{-1} (M-OOH*) confirm H_2O_2 formation [45], while a band at 847 cm^{-1} is assigned to Fe=O (Fe(IV)), a key oxidizing intermediate [4]. Peaks at 1693 and 1683 cm^{-1} correspond to HCO_3^- and COOH* (Figure 3i) [48,49], typical intermediates in H_2O_2 formation from CO, O_2, and H_2O. For methane oxidation, bands at 1716, 1676, 1539, and 1474 cm^{-1} indicate CH_3COO* [46,50], and a band at 1028 cm^{-1} corresponds to OCH_3* (Figure 3h) [51]. These results show that Au/TiO_2 promotes O_2 activation and H_2O_2 formation, while Fe/ZSM-5 catalyzes methane oxidation to oxygenates in the presence of CO.

3.4. Effect of Integrated Manners on Methane Oxidation

The integrated manners of active sites in this tandem catalytic system plays a crucial role in determining the overall reaction performance. To systematically investigate the distance effect between Au/TiO_2 and Fe/ZSM-5 catalysts, we conducted *in situ* synchrotron vacuum ultraviolet photoionization mass spectrometry (SVUV-PIMS) experiments. As illustrated in Figure 4a, three distinct catalyst configurations were prepared by loading 100 mg of 20–40 mesh catalyst into a quartz reactor: (I) dual-bed layered packing configuration (Au/TiO_2 up and Fe/ZSM-5 bottom); (II) granule stacking after pelletization; and (III) mortar mixing before pelletization. Analysis focused on methane oxidation products CH_3OH (*m*/*z* = 32), HCOOH (*m*/*z* = 46), and CH_3COOH (*m*/*z* = 60), correlating with catalytic activity (Figure 4b). Under identical conditions, the mortar-mixed configuration (III) showed significantly stronger signal intensities than the other two. Time-dependent, background-subtracted data confirmed greater product accumulation in all cases, with configuration (III) exhibiting the highest activity (Figure 4c). The superior performance of the mortar-mixed catalyst stems from the minimal distance between active sites, which shortens H_2O_2 diffusion, maximizes its local concentration at Fe sites, and enables immediate activation for methane oxidation before decomposition. The superior performance of the mortar-mixed catalyst stems from the minimal distance between active sites, which shortens H_2O_2 diffusion, maximizes its local concentration at Fe sites, and enables immediate activation for methane oxidation before decomposition, as supported by experiments showing a critical H_2O_2 threshold for oxygenate formation (Figure S20).

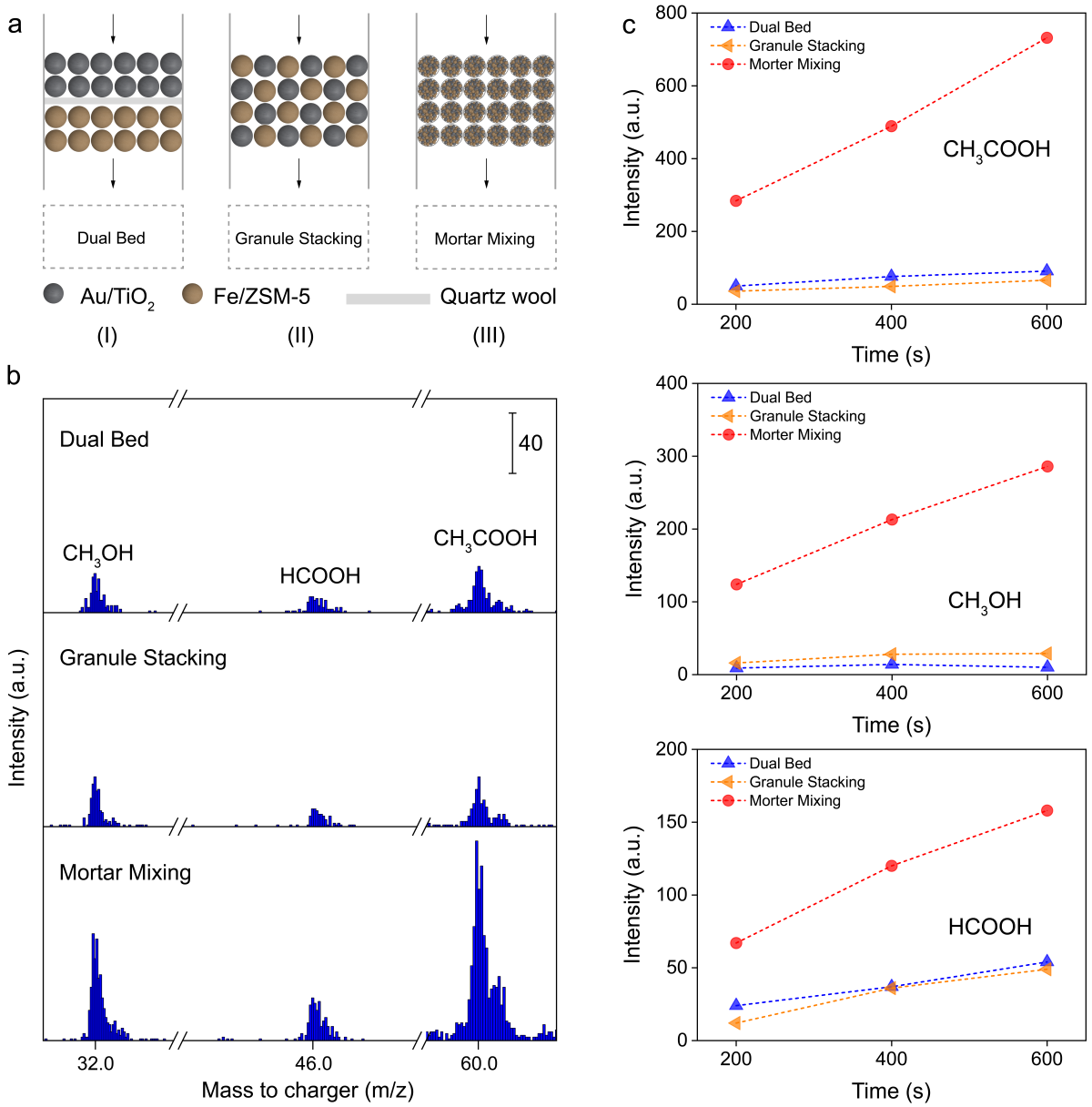

Figure 4. Effect of integrated manners on methane oxidation. (**a**) Detailed integration patterns. (**b**) SVUV-PIMS spectra of reaction intermediates during methane oxidation under the following reaction conditions: total pressure of 2 Torr at 30 °C with 11.5 eV photon energy, using gas flow rates of 15 mL min^{-1} of CH_4, 40 mL min^{-1} of CO, and 6 mL min^{-1} of O_2, where water was introduced by the feed gas. (**c**) Time-accumulated product distribution analysis.

4. Conclusions

In summary, we demonstrated a tandem catalysis system for methane conversion into acetic acid with O_2 in the presence of CO in H_2O solvent at room temperature, without the usage of an external energy source such as light, electricity, or γ-radiation. The process achieved an acetic acid yield of 55.6 μmol g_{cat}^{-1} with a selectivity of 64.9% using the physical mixture of Au/TiO_2 and Fe/ZSM-5 at room temperature. The catalytic efficiency of this tandem system critically depends on the molecular-scale migration of *in situ*-generated H_2O_2 from Au/TiO_2 to Fe/ZSM-5. This close spatial proximity enables immediate activation of H_2O_2 at Fe sites to produce hydroxyl radicals, which drives the reaction toward optimal liquid-phase product formation. Our findings not only add a new dimension to research on the room-temperature conversion of methane, but also deepen our understanding of the proximity effect of multifunctional active sites in heterogeneous catalysis.

Supplementary Materials: The following supporting information can be downloaded at: https://media.sciltp.com/articles/others/2607011053317055/MI-26060083-SM.pdf. Figure S1. XRD patterns of TiO_2 and Au/TiO_2. Figure S2. TEM images for TiO_2 supported Au-based catalysts. (a) Au/TiO_2-A. (b) Au/TiO_2-P25. (c) Au/TiO_2-R. Figure S3. Au 4*f* XPS spectra of Au/TiO_2, Au/TiO_2-A, Au/TiO_2-P25, and Au/TiO_2-R. Figure S4. XRD patterns of ZSM-5 and Fe/ZSM-5. Figure S5. HAADF-STEM characterizations of Fe/ZSM-5-imp. (a) and (b) HAADF-STEM images of Fe/ZSM-5-imp. Figure S6. Fe 2*p* XPS spectra of Fe/ZSM-

5 and Fe/ZSM-5-imp. Figure S7. XAS measurements of Fe foil, Fe_2O_3, Fe/ZSM-5, and Fe/ZSM-5-imp. (a) Normalized Fe *K*-edge XANES spectra. (b) k^3-weighted Fe *K*-edge EXAFS spectra. Figure S8. H_2O_2 synthesis over Au/TiO_2 and Fe/ZSM-5. The reaction was conducted over 15 mg of the catalyst with mechanical stirring (1000 rpm) in 15 mL of H_2O under 40 bar of CO, 6 bar of O_2, and 15 bar of N_2 at 30 °C for 1 h. Figure S9. Standard calibration curves for oxygenates quantification. (a) CH_3OH. (b) HCOOH. (c) CH_3COOH. (d) $HOCH_2OH$. Figure S10. (a) and (b) Typical ^1H NMR and UV-Vis spectra. Figure S11. Methane oxidation with H_2O_2 in the presence of CO over Au/TiO_2 and Fe/ZSM-5. The reaction was conducted over 50 mg of the catalyst with mechanical stirring (1000 rpm) in 15 mL of H_2O containing 1500 μmol of H_2O_2 under 15 bar of CH_4, 40 bar of CO, and 6 bar of N_2 at 30 °C for 1 h. Figure S12. Methane oxidation with H_2O_2 as the oxidant over Au/TiO_2. (a) Remaining H_2O_2 after reaction. (b) Amount of produced oxygenates. The reaction was conducted over 50 mg of Au/TiO_2 with mechanical stirring (1000 rpm) in 15 mL of H_2O containing 50~500 μmol of H_2O_2 under 15 bar of CH_4 and 46 bar of N_2 at 30 °C for 1 h. Figure S13. (a) Catalytic performance and (b) remaining H_2O_2 amount over M/TiO_2 (M= Au, Pd, Pt, Cu) and Fe/ZSM-5. The reaction was conducted over a total catalyst mass of 150 mg with mechanical stirring (1000 rpm) in 15 mL of H_2O under 15 bar of CH_4, 40 bar of CO, and 6 bar of O_2 at 30 °C for 6 h. Figure S14. CH_4 partial pressure-dependent product yields over Au/TiO_2 + Fe/ZSM-5 under a standard condition except for CH_4 partial pressure. The reaction was conducted over 150 mg of Au/TiO_2 + Fe/ZSM-5 with mechanical stirring (1000 rpm) in 15 mL of H_2O under 61 bar containing 3~15 bar of CH_4, 40 bar of CO, 6 bar of O_2, and N_2 as a balanced gas at 30 °C for 6 h. Figure S15. Time-dependent product yields over Au/TiO_2 + Fe/ZSM-5 under a standard condition except for the reaction time. The reaction was conducted over 150 mg of Au/TiO_2 + Fe/ZSM-5 with mechanical stirring (1000 rpm) in 15 mL of H_2O under 15 bar of CH_4, 40 bar of CO, and 6 bar of O_2 at 30 °C for 1~6 h. Figure S16. (a) TEM image and (b) Particle size distribution of Au nanoparticles for physically mixed Au/TiO_2 with Fe/ZSM-5 after fourth *in situ* cycles. (c) Au 4*f* XPS spectra for fresh and spent Au/TiO_2. (d) Fe 3*d* XPS spectra for fresh and spent Fe/ZSM-5. Figure S17. ^1H NMR spectrum for the isotopic labeling experiments. The reaction was conducted over 150 mg of Au/TiO_2 + Fe/ZSM-5 with mechanical stirring (1000 rpm) in 15 mL of H_2O under 8 bar of CH_4 (or 8 bar of $^{13}CH_4$), 8 bar of CO (or 8 bar of ^{13}CO), and 4 bar of O_2 at 30 °C for 6 h. Figure S18. Effect of pH on catalytic performance under standard reaction conditions. HNO_3 and NaOH were used to adjust the pH value of the system. Figure S19. Effect of solvent on catalytic performance over 50 mg of Au/TiO_2 and 100 mg of Fe/ZSM-5 under standard reaction conditions. Figure S20. Methane oxidation with H_2O_2 in the presence of CO over Fe/ZSM-5. The reaction was conducted over 100 mg of Fe/ZSM-5 with mechanical stirring (1000 rpm) in 15 mL of H_2O containing 1.5~50 μmol of H_2O_2 under 15 bar of CH_4, 40 bar of CO, and 6 bar of N_2 at 30 °C for 1 h. Table S1. ICP-AES results of all the samples. Table S2. The deconvolution result of UV-Vis spectra of ZSM-5, Fe/ZSM-5, and Fe/ZSM-5-imp. Table S3. EXAFS fitting results of Fe foil and Fe-containing samples. *CN* refers to the coordination number. *R* refers to the bond length. σ^2 refers to the Debye-Waller factor. ΔE_0 refers to the inner potential correction to account for the difference in the inner potential between the sample and the reference compound. *R*-factor refers to the goodness of fit. Table S4. Adjusting the mass loading of Fe/ZSM-5 (0~100 mg) while maintaining a fixed Au/TiO_2 (15 mg) on methane oxidation. The reaction was conducted over Au/TiO_2 + Fe/ZSM-5 with mechanical stirring (1000 rpm) in 15 mL of H_2O under 15 bar of CH_4, 40 bar of CO, and 6 bar of O_2 at 30 °C for 6 h. Table S5. Adjusting the mass loading of Au/TiO_2 (0~80 mg) while maintaining a fixed Fe/ZSM-5 (100 mg) on methane oxidation. The reaction was conducted over Au/TiO_2 + Fe/ZSM-5 with mechanical stirring (1000 rpm) in 15 mL of H_2O under 15 bar of CH_4, 40 bar of CO, and 6 bar of O_2 at 30 °C for 6 h. Table S6. Mass ratio effect of the Au/TiO_2 to Fe/ZSM-5 on methane oxidation. The reaction was conducted over a total catalyst mass of 150 mg with mechanical stirring (1000 rpm) in 15 mL of H_2O under 15 bar of CH_4, 40 bar of CO, and 6 bar of O_2 at 30 °C for 6 h. Table S7. Comparison of methane oxidation with O_2/H_2O_2 as the oxidants in the presence of CO at low temperatures. Table S8. CO partial pressure-dependent product yields over Au/TiO_2 + Fe/ZSM-5 under a standard condition except for CO partial pressure. The reaction was conducted over 150 mg of Au/TiO_2 + Fe/ZSM-5 with mechanical stirring (1000 rpm) in 15 mL of H_2O under 61 bar containing 15 bar of CH_4, 0~40 bar of CO, 6 bar of O_2, and N_2 as a balanced gas at 30 °C for 6 h. Table S9. CH_4 partial pressure-dependent product yields over Au/TiO_2 + Fe/ZSM-5 under a standard condition except for CH_4 partial pressure. The reaction was conducted over 150 mg of Au/TiO_2 + Fe/ZSM-5 with mechanical stirring (1000 rpm) in 15 mL of H_2O under 61 bar containing 3~15 bar of CH_4, 40 bar of CO, 6 bar of O_2, and N_2 as a balanced gas at 30 °C for 6 h. Table S10. Time-dependent product yields over Au/TiO_2 + Fe/ZSM-5 under a standard condition except for the reaction time. The reaction was conducted over 150 mg of Au/TiO_2 + Fe/ZSM-5 with mechanical stirring (1000 rpm) in 15 mL of H_2O under 15 bar of CH_4, 40 bar of CO, and 6 bar of O_2 at 30 °C for 1~6 h. Table S11. ICP-AES analysis after methane oxidation under standard reaction conditions. References [52–55] are cited in supplementary materials.

Author Contributions: H.L. (Hongfei Lin) and J.Z.: conceived and designed the experiments. H.L. (Hongfei Lin), H.Y., C.M., C.L., L.Z. and H.L. (Hongliang Li): performed the catalyst preparation, characterization, and wrote the manuscript. H.L. (Hongfei Lin), H.Y., and H.L. (Hongliang Li): performed the catalytic tests. H.L. (Hongfei Lin), H.Y., and B.W.: prepared the manuscript and J.Z. and B.W.: revised the writing. The manuscript was written through the contributions of all authors. All authors have read and agreed to the published version of the manuscript.

Funding: This work was supported by National Key Research and Development Program of China (2021YFA1500500), CAS Project for Young Scientists in Basic Research (YSBR-051), NSFC (22525021, 22221003, 22250007, 22504137, 22361162655, 22308346, U25A20545), the Science and Technology Development Fund (FDCT) of Macao S.A.R (0070/2023/AFJ), Fundamental Research Funds for the Central Universities (WK9990250174), Strategic Priority Research Program of the Chinese Academy of Sciences (XDB0450000), Collaborative Innovation Program of Hefei Science Center, CAS (2022HSC-CIP004), the Joint Fund of the Yulin University and the Dalian National Laboratory for Clean Energy (YLU-DNL Fund 2022012), Joint Funds from the Hefei National Synchrotron Radiation Laboratory (KY9990000202, KY9990000900), Special Science and Technology Innovation Program for Carbon Peak and Carbon Neutralization of Jiangsu Province (Grant No. BE2025014), USTC Research Funds of the Double First-Class Initiative (YD9990002014), the Anhui Natural Science Foundation for Young Scholars (2408085QB047), University of Science and Technology of China-Xinjiang Normal University Counterpart Cooperation and Development Joint Fund (KY9990002504), and International Partnership Program of Chinese Academy of Sciences (123GJHZ2022101GC). J.Z. acknowledges support from the Tencent Foundation through the XPLORER PRIZE. This work was partially carried out at the Instruments Center for Physical Science, University of Science and Technology of China. This work was also partially carried out at the USTC Center for Micro and Nanoscale Research and Fabrication.

Data Availability Statement: Data are available from the corresponding author upon reasonable request.

Conflicts of Interest: The authors declare no conflict of interest.

Use of AI and AI-Assisted Technologies: No AI tools were utilized for this paper.

References

1. Agarwal, N.; Freakley, S.; McVicker, R.; Althahban, S.; Dimitratos, N.; He, Q.; Morgan, D.; Jenkins, R.; Willock, D.; Taylor, S.; et al. Aqueous Au-Pd colloids catalyze selective CH_4 oxidation to CH_3OH with O_2 under mild conditions. *Science* **2017**, *358*, 223–227.
2. Schwach, P.; Pan, X.; Bao, X. Direct conversion of methane to value-added chemicals over heterogeneous catalysts: Challenges and prospects. *Chem. Rev.* **2017**, *117*, 8497–8520.
3. Yu, B.; Chen, L.; Wu, J.; Yang, B.; Li, H.; Xu, J.; Zhang, Y.; Pan, C.; Cao, X.; Zhu, Y.; et al. Surface hydroxyl group dominating aerobic oxidation of methane below room temperature. *Energy Environ. Sci.* **2024**, *17*, 8127–8139.
4. Shen, W.; Yao, C.; Yu, B.; Ge, S.; Tang, X.; Xu, J.; Zhang, Y.; Pan, C.; Zhu, Y.; Lou, Y. Synergistic catalysis over Fe-Cu dual single-atom sites boosting direct oxidation of methane to C1 oxygenates. *Chem. Eng. J.* **2026**, *528*, 172245.
5. Banerjee, R.; Proshlyakov, Y.; Lipscomb, J.; Proshlyakov, D. Structure of the key species in the enzymatic oxidation of methane to methanol. *Nature* **2015**, *518*, 431–434.
6. Koo, C.; Tucci, F.; He, Y.; Rosenzweig, A. Recovery of particulate methane monooxygenase structure and activity in a lipid bilayer. *Science* **2022**, *375*, 1287–1291.
7. Tucci, F.; Jodts, R.; Hoffman, B.; Rosenzweig, A. Product analogue binding identifies the copper active site of particulate methane monooxygenase. *Nat. Catal*. **2023**, *6*, 1194–1204.
8. Mao, J.; Liu, H.; Cui, X.; Zhang, Y.; Meng, X.; Zheng, Y.; Chen, M.; Pan, Y.; Zhao, Z.; Hou, G.; et al. Direct conversion of methane with O_2 at room temperature over edge-rich MoS_2. *Nat. Catal*. **2023**, *6*. 1052–1061.
9. Wang, S.; Fung, V.; Hülsey, M.; Liang, X.; Yu, Z.; Chang, J.; Folli, A.; Lewis, R.; Hutchings, G.; He, Q.; et al. H_2-reduced phosphomolybdate promotes room-temperature aerobic oxidation of methane to methanol. *Nat. Catal*. **2023**, *6*, 895–905.
10. Qi, G.; Davies, T.; Nasrallah, A.; Sainna, M.; Howe, A.; Lewis, R.; Quesne, M.; Catlo, C.; Willock, D.; He, Q.; et al. Au-ZSM-5 catalyses the selective oxidation of CH_4 to CH_3OH and CH_3COOH using O_2. *Nat. Catal.* **2022**, *5*, 45–54.
11. Shan, J.; Li, M.; Allard, L.; Lee, S.; Flytzani-Stephanopoulos, M. Mild oxidation of methane to methanol or acetic acid on supported isolated rhodium catalysts. *Nature* **2017**, *551*, 605–608.
12. Tang, Y.; Li, Y.; Fung, V.; Jiang, D.; Huang, W.; Zhang, S.; Iwasawa, Y.; Sakata, T.; Nguyen, L.; Zhang, X.; et al. Single rhodium atoms anchored in micropores for efficient transformation of methane under mild conditions. *Nat. Commun.* **2018**, *9*, 1231.
13. Li, H.; Fei, M.; Troiano, J.; Ma, L.; Yan, X.; Tieu, P.; Yuan, Y.; Zhang, Y.; Liu, T.; Pan, X.; et al. Selective methane oxidation by heterogenized iridium catalysts. *J. Am. Chem. Soc.* **2023**, *145*, 769–773.
14. Wu, B.; Lin, T.; Lu, Z.; Yu, X.; Huang, M.; Yang, R.; Wang, C.; Tian, C.; Li, J.; Sun, Y.; et al. Fe binuclear sites convert methane to acetic acid with ultrahigh selectivity. *Chem* **2022**, *8*, 1658–1672.
15. Cheng, Q.; Yao, X.; Li, G.; Li, G.; Zheng, L.; Yang, K.; Emwas, A.; Li, X.; Han, Y.; Gascon, J. Atomically dispersed iron-copper dual-metal sites synergistically boost carbonylation of methane. *Angew. Chem. Int. Ed.* **2024**, *136*, e202411048.
16. Xu, W.; Liu, H.; Hu, Y.; Wang, Z.; Huang, Z.; Huang, C.; Lin, J.; Chang, C.; Wang, A.; Wang, X.; et al. Metal-oxo electronic tuning via *in situ* CO decoration for promoting methane conversion to oxygenates over single-atom catalysts. *Angew. Chem. Int. Ed.* **2024**, *136*, e202315343.
17. Reis, P.; da Silva, J.; Palavra, A.; da Silva, J.; Kitamura, T.; Fujiwara, Y.; Pombeiro, A. Single-pot conversion of methane into acetic acid in the absence of CO and with vanadium catalysts such as amavadine. *Angew. Chem. Int. Ed.* **2003**, *115*, 845–847.
18. Kirillova, M.; Kuznetsov, M.; Reis, P.; da Silva, J.; da Silva, J.; Pombeiro, A. Direct and remarkably efficient conversion of methane into acetic acid catalyzed by amavadine and related vanadium complexes. *J. Am. Chem. Soc.* **2007**, *129*, 10531–10545.
19. Antil, N.; Chauhan, M.; Akhtar, N.; Kalita, R.; Manna, K. Selective methane oxidation to acetic acid using molecular oxygen over a mono-copper hydroxyl catalyst. *J. Am. Chem. Soc.* **2023**, *145*, 6156–6165.
20. Gupta, P.; Chauhan, M.; Rana, B.; Kalita, R.; Maurya, R.; Manna, K. Engineering mono-vs dinuclear iron(II)-active sites to steer liquid oxygenate selectivity in methane oxidation pathways using O_2. *J. Am. Chem. Soc.* **2025**, *147*, 25372–25384.
21. Gupta, P.; Rana, B.; Maurya, R.; Kalita, R.; Chauhan, M.; Manna, K. Copper catalyzed selective methane oxidation to acetic acid using O_2. *Chem. Sci.* **2025**, *16*, 2785–2795.
22. Yu, B.; Li, W.; Tang, X.; Cheng, L.; Zhang, J.; Yang, S.; Liu, F.; Xu, J.; Zhang, Y.; Pan, C.; et al. Fe-(μ-O)-Zn dual-atom boosting C-C coupling for direct oxidation of methane to acetic acid using O_2. *Nat. Commun.* **2025**, *16*, 9471.

23. Dong, C.; Marinova, M.; Tayeb, K.; Safonova, O.; Zhou, Y.; Hu, D.; Chernyak, S.; Corda, M.; Zaffran, J.; Khodakov, A.; et al. Direct photocatalytic synthesis of acetic acid from methane and CO at ambient temperature using water as oxidant. *J. Am. Chem. Soc.* **2023**, *145*, 1185–1193.
24. Wang, L.; Yi, Y.; Wu, C.; Guo, H.; Tu, X. One-step reforming of CO_2 and CH_4 into high-value liquid chemicals and fuels at room temperature by plasma-driven catalysis. *Angew. Chem. Int. Ed.* **2017**, *129*, 13867–13871.
25. Huang, F.; Sun, X.; Liu, Y.; Huang, W. Water radiocatalysis for selective aqueous-phase methane carboxylation with carbon dioxide into acetic acid at room temperature. *J. Am. Chem. Soc.* **2024**, *146*, 8492–8499.
26. Lu, P.; Zhao, Y.; Dong, J.; Mei, B.; Du, X.; Jiang, Z.; Liu, Y.; He, H.; Wang, Y.; Duan, X.; et al. Direct and efficient synthesis of clean H_2O_2 from CO-assisted aqueous O_2 reduction. *ACS Catal.* **2020**, *10*, 13993–14005.
27. Yuan, W.; Zhu, B.; Fang, K.; Li, X.; Hansen, T.; Ou, Y.; Yang, H.; Wagner, J.; Gao, Y.; Wang, Y.; et al. *In situ* manipulation of the active Au-TiO_2 interface with atomic precision during CO oxidation. *Science* **2021**, *371*, 517–521.
28. Li, X.; Xi, Y.; Liu, Q.; Bahri, M.; Zhang, L.; Browning, N.; Cowan, A.; Tang, J. Efficient hole abstraction for highly selective oxidative coupling of methane by Au-sputtered TiO_2 photocatalysts. *Nat. Energy* **2023**, *8*, 1013–1022.
29. Murdoch, M.G.; Waterhouse, G.I.N.; Naddem, M.A.; Metson, J.B.; Keane, M.A.; Howe, R.F.; Llorca, J.; Idriss, H. The effect of gold loading and particle size on photocatalytic hydrogen production from ethanol over Au/TiO_2 nanoparticles. *Nat. Chem* **2011**, *3*, 489–492.
30. Zhang, Y.; Liu, J.; Qian, K.; Jia, A.; Li, D.; Shi, L.; Hu, J.; Zhu, J.; Huang, W. Structure sensitivity of Au-TiO_2 strong metal–support interactions. *Angew. Chem. Int. Ed.* **2021**, *60*, 12074–12081.
31. Zhu, Y.; Li, Z.; Bian, J.; Zhang, Z.; Chen, C.; Xiong, L.; Tang, J.; Jing, L. Highly selective photo-oxidation of methane to methanol by Fe–Au site-supported $SrTiO_3$ hollow nanotubes with oxygen vacancies. *J. Am. Chem. Soc.* **2025**, *147*, 34959–34971.
32. Zhao, S.; Liu, M.; Qu, Z.; Yan, Y.; Zhang, Z.; Yang, J.; He, S.; Xu, Z.; Zhu, Y.; Luo, L.; et al. Cascade synthesis of Fe-N_2-Fe dual-atom catalysts for superior oxygen catalysis. *Angew. Chem. Int. Ed.* **2024**, *63*, e202408914.
33. Zhou, Y.; Zhang, J.; Wang, L.; Cui, X.; Liu, X.; Wong, S.; An, H.; Yan, N.; Xie, J.; Yu, C.; et al. Self-assembled iron-containing mordenite monolith for carbon dioxide sieving. *Science* **2021**, *373*, 315–320.
34. Zhu, K.; Liang, S.; Cui, X.; Huang, R.; Wan, N.; Hua, L.; Li, H.; Chen, H.; Zhao, Z.; Hou, G.; et al. Highly efficient conversion of methane to formic acid under mild conditions at ZSM-5-confined Fe-sites. *Nano Energy* **2021**, *82*, 105718.
35. Cheng, Q.; Li, G.; Yao, X.; Zheng, L.; Wang, J.; Emwas, A.; Castaño, P.; Ruiz-Martínez, J.; Han, Y. Maximizing active Fe species in ZSM-5 zeolite using organic-template-free synthesis for efficient selective methane oxidation. *J. Am. Chem. Soc.* **2023**, *145*, 5888–5898.
36. Wang, C.; Sun, Y.; Wang, L.; Feng, W.; Miao, Y.; Yu, M.; Wang, Y.; Gao, X.; Zhao, Q.; Ding, Z.; et al. Oxidative carbonylation of methane to acetic acid on an Fe-modified ZSM-5 zeolite. *Appl Catal. B Environ.* **2023**, *329*, 122549.
37. Yu, X.; Wu, B.; Huang, M.; Lu, Z.; Li, J.; Zhong, L.; Sun, Y. IrFe/ZSM-5 synergistic catalyst for selective oxidation of methane to formic acid. *Energy Fuels* **2021**, *35*, 4418–4427.
38. Li, W.; Li, Z.; Zhang, H.; Liu, P.; Xie, Z.; Song, W.; Liu, B.; Zhao, Z. Efficient catalysts of surface hydrophobic Cu-BTC with coordinatively unsaturated Cu(I) sites for the direct oxidation of methane. *Proc. Natl. Acad. Sci. USA* **2023**, *120*, e2206619120.
39. Li, H.; Xiong, C.; Fei, M.; Ma, L.; Zhang, H.; Yan, X.; Tieu, P.; Zhang, Y.; Nyakuchena, J.; Huang, J.; et al. Selective formation of acetic acid and methanol by direct methane oxidation using rhodium single-atom catalysts. *J. Am. Chem. Soc.* **2023**, *145*, 11415–11419.
40. Song, X.; Basheer, C.; Zare, R. Water microdroplets-initiated methane oxidation. *J. Am. Chem. Soc.* **2023**, *145*, 27198–27204.
41. Shen, Q.; Cao, C.; Huang, R.; Zhu, L.; Zhou, X.; Zhang, Q.; Gu, L.; Song, W. Single chromium atoms supported on titanium dioxide nanoparticles for synergic catalytic methane conversion under mild conditions. *Angew. Chem. Int. Ed.* **2020**, *59*, 1216–1219.
42. Li, M.; Sen, A. Direct catalytic conversion of methane to acetic acid in an aqueous medium. *Nature* **1994**, *368*, 613–615.
43. Zhang, W.; Xi, D.; Chen, Y.; Chen, A.; Jiang, Y.; Liu, H.; Zhou, Z.; Zhang, H.; Liu, Z.; Long, R.; et al. Light-driven flow synthesis of acetic acid from methane with chemical looping. *Nat. Commun.* **2023**, *14*, 3047.
44. Mu, B.; Zhang, Y.; Peng, M.; Tu, Z.; Guo, Z.; Shen, S.; Xu, Y.; Liang, W.; Wang, X.; Wang, M.; et al. Radiocatalytic synthesis of acetic acid from CH_4 and CO_2. *Angew. Chem. Int. Ed.* **2024**, *63*, e202407443.
45. Wang, W.; Zhou, W.; Tang, Y.; Cao, W.; Docherty, S.; Wu, F.; Cheng, K.; Zhang, Q.; Copéret, C.; Wang, Y. Selective oxidation of methane to methanol over Au/H-MOR. *J. Am. Chem. Soc.* **2023**, *145*, 12928–12934.
46. Wu, B.; Yin, H.; Ma, X.; Liu, R.; He, B.; Li, H.; Zeng, J. Highly selective synthesis of acetic acid from hydroxyl-mediated oxidation of methane at low temperatures. *Angew. Chem. Int. Ed.* **2025**, *64*, e202412995.
47. Wu, B.; Lin, T.; Huang, M.; Li, S.; Li, J.; Yu, X.; Yang, R.; Sun, F.; Jiang, Z.; Sun, Y.; et al. Tandem catalysis for selective oxidation of methane to oxygenates using oxygen over PdCu/Zeolite. *Angew. Chem. Int. Ed.* **2022**, *61*, e202204116.

48. Fedorova, E.; Kraußer, M.; Weiß, J.; Fedorov, M.; Brückner, A.; Kondratenko, E.; Kubis, C. Operando DRIFTS Investigations on surface intermediates and effects of potassium in CO_2 hydrogenation over a K-Fe/$YZrO_x$ catalyst. *ChemCatChem* **2024**, *16*, e202301697.
49. Kar, T.; Scheiner, S.; Roy, A.K.; Bettinger, H.F. Unusual low-vibrational C=O mode of COOH can distinguish between carboxylated zigzag and armchair single-wall carbon nanotubes. *J. Phys. Chem. C* **2012**, *116*, 26072–26083.
50. Zhao, X.; Yin, H.; Lin, H.; Dai, Z.; Chen, X.; We, W.; Li, H.; Wu, B.; Zeng, J. The importance of Si-ONa-Al moieties in Fe/ZSM-5 zeolite catalysts for selective oxidation of methane to acetic acid. *Angew. Chem. Int. Ed.* **2025**, *64*, e202511056.
51. Huang, M.; Zhang, S.; Wu, B.; Wei, Y.; Yu, X.; Gan, Y.; Lin, T.; Yu, F.; Sun, F.; Jiang, Z.; et al. Selective photocatalytic oxidation of methane to oxygenates over Cu-W-TiO_2 with significant carrier traps. *ACS Catal.* **2022**, *12*, 9515–9525.
52. Gu, F.; Qin, X.; Pang, L.; Zhang, R.; Peng, M.; Xu, Y.; Hong, S.; Xie, J.; Wang, M.; Han, D.; et al. Acid-promoted selective oxidation of methane to formic acid over dispersed rhodium catalysts under mild conditions. *ACS Catal.* **2023**, *13*, 9509–9514.
53. Gu, F.; Qin, X.; Li, M.; Xu, Y.; Hong, S.; Ouyang, M.; Giannakakis, G.; Cao, S.; Peng, M.; Xie, J.; et al. Selective catalytic oxidation of methane to methanol in aqueous medium over copper cations promoted by atomically dispersed rhodium on TiO_2. *Angew. Chem. Int. Ed.* **2022**, *61*, e202201540.
54. Mao, J.; Liu, H.; Li, Y.; Gao, M.; Zhang, Y.; Song, Y.; Zhang, M.; Xu, G.; Zhou, W.; Yu, L.; et al. Mild-condition conversion of methane to acetic acid over MoS_2-confined Rh-Fe sites. *J. Am. Chem. Soc.* **2025**, *147*, 14530–14540.
55. Liu, J.; Wei, Y.; Li, R.; Liu, Y.; Yu, H.; Zhou, X.; Wu, B.; Lin, T.; Zhong, L. Isolated Ni sites anchored on zeolites for direct synthesis of acetic acid from methane oxidative carbonylation. *Appl. Catal. B* **2024**, *350*, 123951.